

A novel bone suppression method that improves lung nodule detection

Suppressing dedicated bone shadows in radiographs while preserving the remaining signal

Jens von Berg¹ · Stewart Young¹ · Heike Carolus¹ · Robin Wolz² · Axel Saalbach¹ · Alberto Hidalgo³ · Ana Giménez³ · Tomás Franquet³

Received: 20 January 2015 / Accepted: 30 July 2015 / Published online: 4 September 2015
© CARS 2015

Abstract

Purpose Suppressing thoracic bone shadows in chest radiographs has been previously reported to improve the detection rates for solid lung nodules, however at the cost of increased false detection rates. These bone suppression methods are based on an artificial neural network that was trained using dual-energy subtraction images in order to mimic their appearance.

Method Here, a novel approach is followed where all bone shadows crossing the lung field are suppressed sequentially leaving the intercostal space unaffected. Given a contour delineating a bone, its image region is spatially transferred to separate normal image gradient components from tangential component. Smoothing the normal partial gradient along the contour results in a reconstruction of the image representing the bone shadow only, because all other overlaid signals tend to cancel out each other in this representation.

Results The method works even with highly contrasted overlaid objects such as a pacemaker. The approach was validated in a reader study with two experienced chest radiologists, and these images helped improving both the sensitivity and the specificity of the readers for the detection and localization of solid lung nodules. The AUC improved significantly from 0.596 to 0.655 on a basis of 146 images from patients and normals with a total of 123 confirmed lung nodules.

Conclusion Subtracting all reconstructed bone shadows from the original image results in a *soft image* where lung nodules are no longer obscured by bone shadows. Both the sensitivity and the specificity of experienced radiologists increased.

Keywords Bone suppression · Thorax · Radiography · Lung nodule

Introduction

Lung cancer is a major cause of death both in industrialized and in newly industrialized countries. Early diagnosis is the key to cure lung cancer. While screening for lung cancer with medical imaging is still under debate in many of the concerned countries, many lung nodule cases are currently diagnosed incidentally by CT or by chest radiography. The sensitivity of chest radiography for lung nodule detection is not as high as that of other modalities such as chest CT, chest tomosynthesis or dual-energy subtraction radiography. However, its very high availability and the large numbers of examinations—more than any other modality—make it an important diagnostic means to detect lung cancer.

In X-ray projection images, the overlay of different anatomical structures is an inherent problem that impacts reading these images. Positioning the patient well is important to minimize this effect. Still, important anatomical findings may be covered by bones, rendering them difficult to detect. For chest radiography, which is the most frequently performed medical image, the thoracic bones in particular hold the risk of covering critical small opacities in the lung. In practice, this accounts for a high portion of missed lung nodules [19].

✉ Jens von Berg
jens.von.berg@philips.com

¹ Digital Imaging, Philips Research, Hamburg, Germany

² Clinical Science, Diagnostix X-Ray, Philips Healthcare, Hamburg, Germany

³ Department of Radiology, Hospital de la Santa Creu i Sant Pau, Carrer de Sant Quintí, 89, Barcelona, Spain

In a digital chest radiography, a thoracic bone does not reduce the X-ray signal to such an extent that other signals on the projection line are fully shadowed. Modern detectors have a dynamic range that allows the detection of these small opacities, even when they are overlaid with a bone. Therefore the image can be considered as a sum of absorption values from all objects present in the projection line toward a single image pixel. Intrinsically, the task of separating these signals from each other is under-determined for a single given projection. By exploiting some existing coherence in the image, it is possible to approximate a separation of the bone signal from the rest and calculate the *soft image* by $I_{\text{soft}} = I - I_{\text{bone}_1} - I_{\text{bone}_2} \dots - I_{\text{bone}_n}$. This article outlines a novel approach to estimating the soft image as well as the bone images and reports improved lung nodule detection by some experienced radiologists when provided with such a soft image.

Bone suppression has been proposed to be applied in different medical diagnostic tasks. First, it was applied to preprocess follow-up radiographs in order to improve the quality of temporal subtraction images [9]. Then it turned out to be a value of its own. There are some studies showing the benefit in improving the lung nodule detection characteristics for radiologist when reading an additional soft image [4, 12, 13, 18, 23]. The applicability to support detection of focal pneumonia showing a similar appearance to solid lung nodules has been shown in [11]. Another study has addressed the effect of bone suppression on the detection of pulmonary aspergillosis [17]. They all agree in an enlarged area under the ROC curve (AUC); however, the specificity for the detection decreased by the use of bone suppression, thus giving both more true and more false positive findings than with the original radiograph alone. All these studies are based on an implicit method for bone suppression trained from dual-energy subtraction images (see below).

Another important application is to use bone suppression as preprocessing for a lung nodule computer-aided detection (CAD) software. It may help rule out false positives that often erroneously occur at rib or clavicle crossings, but may also help to improve selectivity for opacities previously masked by bone shadows. This is motivated for lung nodule detection in [8] and in another context for ruling out tuberculosis in [6]. In [15], an improvement, however not statistically significant, could be observed for a lung nodule CAD based on bone suppression. Application proposals outside diagnostics are rare. In [24], bone suppression is proposed to improve image-guided radiation therapy planning in biplanar fluoroscopy.

Approaches in the literature to retrospectively suppress the thoracic bone shadows in radiographs may be divided into those explicitly representing the bones or at least some of their edges, and those suppressing their contrast without any explicit spatial representation. The latter may be referred to as implicit methods. The implicit methods try to separate the image signal into one bone signal and the remaining soft

signal on a pixel by pixel basis. This can be done by supervised machine learning trained with dual-energy subtraction images. In [22], an artificial neural network was used for this purpose, and in [14] a regression technique on pixel basis. These methods rely on training images and aim at mimicking their appearance. Also unsupervised methods have been applied, like a blind source separation approach using an independent component analysis in [1]. This approach has to model the discrimination between bones and the rest of the image without any training data. As there is no explicit separation in the implicit methods between ribs and intercostal space, there is no guarantee that the intercostal space is not modified.

The explicit methods need to delineate the bones and then estimate their contribution to the image intensity, i.e., the bone absorption during the image acquisition. This estimate may be based on some shape parameters given by the segmentation. In an early approach [25], a straightforward rib absorption model was constructed and aligned with the posterior ribs segmented roughly in the image. In [21], the clavicle was suppressed by damping vertical gradients in the local image under the assumption that the clavicle is oriented horizontally. A smoothness constraint of this gradient is introduced in the horizontal extent. This method has been later applied to posterior ribs as well [16] still assuming predominant horizontal extensions of their borders. All these methods address only parts of the thoracic bones and do not show subtraction images of convincing quality. In [7], the approach has been applied to both posterior and anterior ribs also following their main orientation although limited details are given regarding how to exactly form the bone image. In [10], posterior ribs are segmented and a contrast model is applied optimized by some genetic algorithms. In [5, 6], work is reported using perpendicular profiles centered at the rib along the centerline. This method is able to follow a bending rib shadow well, but it was applied to the posterior ribs only, probably because their thickness does not vary significantly along the length of the projection shadow. These profiles are clustered to rule out outliers and then smoothed to approximate the rib absorption. None of these publications provide a general method applicable to all thoracic bones.

In the following “Methods” section, a novel method for bone suppression is introduced. It is designed to improve the detection of lung nodules. In the subsequent section “Technical validation: the impact of bone suppression on lung nodule contrast” variations of this method are examined in order to optimally improve the visibility of lung nodules in the image. In the “Clinical validation” section, the design of a clinical reader study is presented to evaluate the impact of the bone suppression method on the sensitivity as well as on the specificity of experienced chest radiologist for lung nodule detection and localization. In “Results” statistical statements on the outcome of the study are made, and in the “Discus-

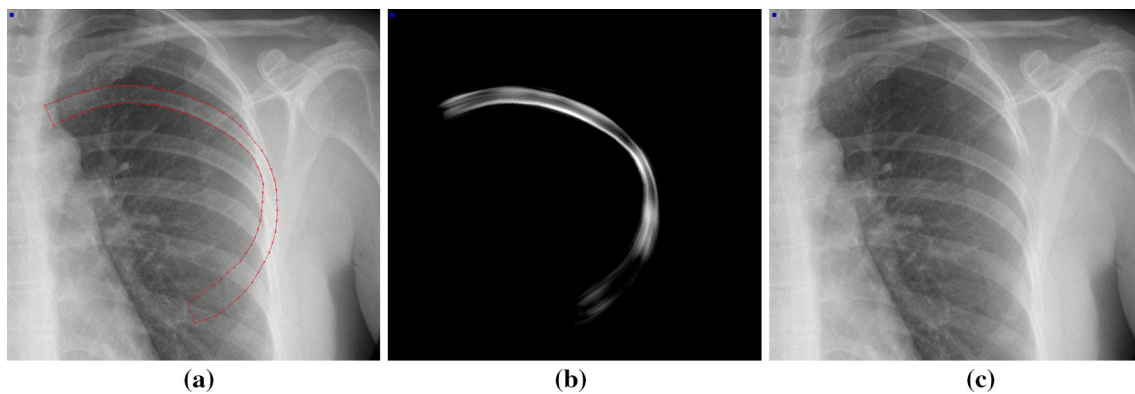


Fig. 1 The bone suppression algorithm removes the bone signal from an image, shown exemplary for fifth rib. **a** Original image with fifth rib. **b** Bone image for fifth rib. **c** Original image without fifth rib

sion” section this reader study and its results are critically reviewed. Also some interesting effects of the bone suppression technique on selected study cases are discussed. In the “Conclusion” section some final statements are made.

Methods

The fundamental idea of the bone suppression algorithm presented in this paper is to remove the shadows of the bones in the original image as visualized in Fig. 1 in order to improve a radiologist’s capability to reliably identify lung nodules in chest radiographs. To this end, each bone overlapping with the lung field, represented by its contour, is transformed into the so-called ST-space where the contour appears as a straight line. This is applied to the ribs and the clavicles. In the ST-space, a partial derivative across the bone contour is computed, smoothed along the contour and then reintegrated up to the centerline. The idea of the smoothing is to remove all other signals besides the bone contour from the image. When reintegrating, only the bone signal is restored and the subtraction of this bone image from the original image results in a visual removal of the bone whose shadow is represented by the contour. Figure 2 shows an overview of the main steps of the bone suppression, which are described in more detail in the following subsections.

ST-transformation

The *ST-transformation*

$$T_C : (x, y) \mapsto (s, t) \quad (1)$$

is a space transformation used to generate a specific representation of a part of the image defined by the given closed contour $C : \gamma(t), t \in [0, C_{\text{len}}]$ with $\gamma(0) = \gamma(C_{\text{len}})$. The contour start point is defined at any point $P_0 = \gamma(0)$. T_C will be introduced by its inverse

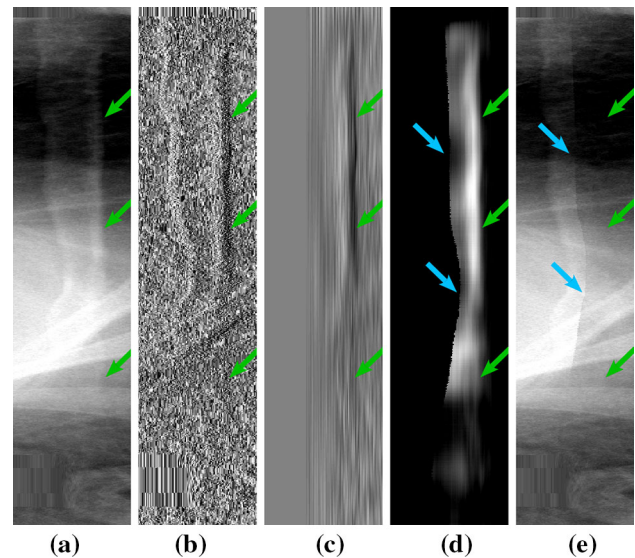


Fig. 2 Main elements of the bone suppression algorithm applied to the fifth rib in the image I as shown in Fig. 1a. **a** Image I transformed into the ST-space of the fifth rib (selected region). Its outer contour at $s = 0$ is marked with green arrows. **b** Partial derivative $\partial s I$. **c** Smoothed image I_s . **d** The reintegration I_r of the smoothed image gives the bone signal. Note that processing is restricted to the left side by the rib centerline (blue arrows)! **e** $I_{\text{soft}} = I - I_r$, still processing is restricted by the rib centerline leaving the irrelevant contralateral part beyond unchanged. Its transformation back into image space results in Fig. 1c

$$T_C^{-1} : (s, t) \mapsto (x, y) \quad (2)$$

which is given by

$$T_C^{-1}(s, t) = \gamma(t) + s \cdot \frac{\gamma'(t)^\perp}{|\gamma'(t)|} \quad (3)$$

where $\frac{\gamma'(t)^\perp}{|\gamma'(t)|}$ is the contour normal at contour point $\gamma(t)$. Figure 3 shows the transformation with respect to the contour C . T_C can be defined as

$$(s_i, t_i) \mid T_C^{-1}(s_i, t_i) = (x, y), i = \arg \min |s_i|. \quad (4)$$

Figure 4 illustrates this with examples.

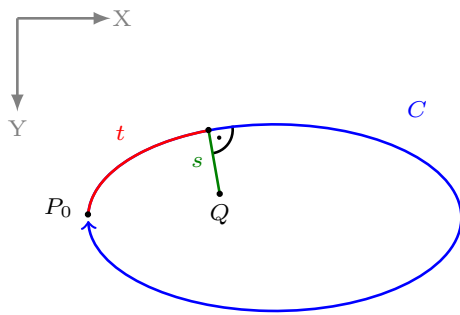


Fig. 3 ST-transformation of point Q with respect to the contour C

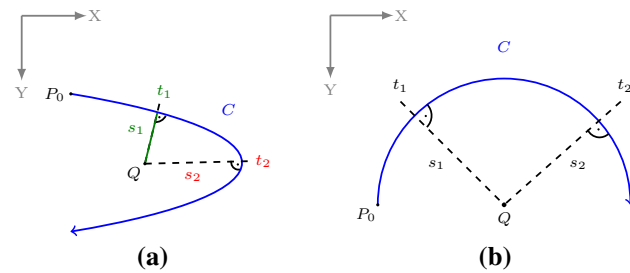


Fig. 4 Ambiguities in the ST-transformation. **a** The potential ambiguity problem of multiple line segments intersecting at Q can be resolved by (4) as only one t -position has a minimal distance to Q . Here $|s_1| < |s_2|$. **b** Equal curvature along the contour leads to a singularity with Q having equal distances to several t -positions. This ambiguity cannot be resolved by (4)

Discrete implementation of the ST-transformation

In the bone suppression prototype, bone contours are represented as piecewise linear closed contours. The ST-transformation is a time critical part of the algorithm, and thus an optimized implementation is required to make it run fast. We use a discrete sampling of the ST-space. As the contour C is closed, the ST-space is cyclic such that

$$(s, 0) = (s, C_{\text{len}}), \quad (5)$$

with C_{len} being the length of the contour C . The s -margin is defined in image space by $s \in [s_{\text{min}}, s_{\text{max}}]$ where s_{min} defines the width of the image to be transformed inside C and s_{max} defines the width outside C . Typical settings are $s_{\text{max}} = 1.7 \text{ mm}$ and $s_{\text{min}} = 20 \text{ mm}$, which should at least be half the thickness of the bone in order to cover it fully.

In the discrete implementation of (1), the (s, t) -coordinates are determined by first finding the edge $e_c \in C$ closest to a point Q and then projecting Q onto this edge. Thereafter, both s and t can be readily determined.

This is illustrated in Fig. 5. At both corners P_1 and P_2 of the edge e_c , the bisecting line of the angle at that corner is constructed and a line parallel to e_c is drawn that intersects with Q . The (s, t) -coordinates can now be computed by:

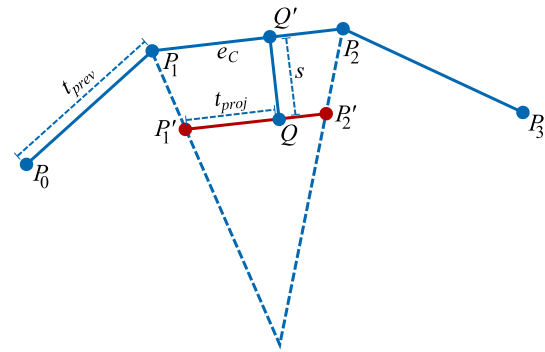


Fig. 5 The discrete ST-transformation of point Q

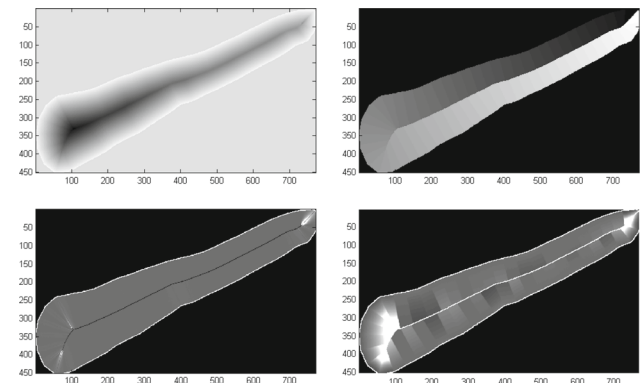


Fig. 6 Properties of the space transformation T when applied to a clavicle contour C . The background outside the margin s_{max} is unaffected and set to zero. *Top left* image coding $(T_C(\mathbf{x})) \cdot s$ for every position \mathbf{x} . *Top right* image coding $(T_C(\mathbf{x})) \cdot t$. The wrap-around at $t = 0 = C_{\text{len}}$ is clearly visible at the top right of the image. *Bottom left* image coding $\partial (T_C(\mathbf{x})) \cdot s$. We observe a ridge with $\partial s = 0$ at the centerline. There are some discontinuities at areas with a high curvature of C . The wrap-around at $t = 0$ also appears as a discontinuity here. *Bottom right* image coding $\partial (T_C(\mathbf{x})) \cdot t$. Due to the foreshortening inside the bone at convex segments, the partial derivative of t increases here (bright areas), but decreases outside. At concave segments, it is just the opposite

$$s = s_{\text{sign}} \|Q - Q'\|$$

$$t = t_{\text{prev}} + \|Q - P'_1\| \frac{\|P_2 - P_1\|}{\|P'_2 - P'_1\|},$$

where t_{prev} is the summed length of all previous edges. The $s_{\text{sign}} \in \{-1, 1\}$ is determined by an inside–outside algorithm of Q with respect to C : negative inside the contour and positive outside. In Fig. 6, some properties of the transformation T_C for a left clavicle are illustrated.

Figure 7 shows an exemplary image of the ST-space of a rib. The inner and outer contours of the rib as well as crossing ribs are clearly visible.

Image construction and inverse ST-transformation

In order to construct an ST-transformed image I_{STC} of a bone, the inverse transformation T_C^{-1} is required as the image intensity in the ST-space is given by

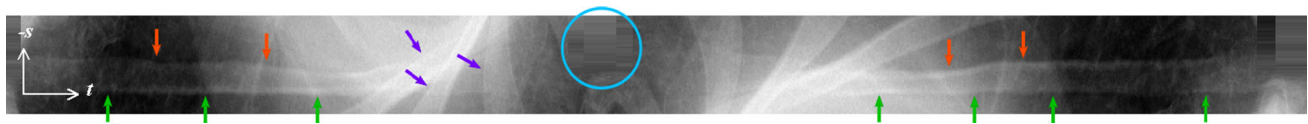


Fig. 7 Full ST-space of the fifth left rib from the example shown in Fig. 2 (presented *horizontally* here). Clearly visible is the contour (green arrows) of the rib at $s = 0$. From *left to right*, it follows the outer contour from the sternum to the tip of the rib and back along the inner contour to the sternum. At the turning point at the medial ending of the anterior rib shadow, the ST-image exhibits artifacts (blue circle) for those

positions with high negative s coordinates. Also the opposite contour of the rib (orange arrows) can be seen. For both structures, however, their representation in the ST-image is not relevant for subsequent signal reconstruction, since these locations lie beyond the centerline of the bone (see “ST-transformation” section). Some crossing ribs (purple arrows) can be seen as well

$$I_{stC}(s, t) = I\left(T_C^{-1}(s, t)\right) \quad (6)$$

using (3). A position (s', t') on the other side of the bone centerline $c(t')$, i.e., with $s' < c(t')$, is considered a *ghost image* of $T_C^{-1}(s', t')$. For every *ghost image* (s', t') , there is a valid (s, t) with $T_C^{-1}(s, t) = T_C^{-1}(s', t')$ and $s \geq c(t)$. The centerline $c(t)$ can be obtained as follows. Considering calculating

$$(\hat{s}, \hat{t}) = T_C\left(T_C^{-1}(s, t)\right), \quad (7)$$

one will find that $(\hat{s}, \hat{t}) \neq (s, t)$ for all negative s -positions (i.e., inside the contour) beyond the centerline (see also “Reintegrate the gradient image” section). The centerline could thus be given as $(c(t), t)$ where

$$c(t) = \max_s \forall (\hat{s}, \hat{t}) \neq (s, t). \quad (8)$$

Partial derivative in ST-space

The partial derivative

$$I_{dC}(s, t) = \partial s I_{stC}(s, t) \quad (9)$$

is realized numerically by the asymmetric difference

$$\partial s I(s, t) = I(s, t) - I(s - 1, t) \quad (10)$$

which represents the gradient orthogonal to the bone main axis. As the bone edge itself is oriented this way, it contributes significantly to I_{dC} . Any structure oriented orthogonal to the bone edge does not contribute to I_{dC} . More generally, any edge oriented with an angle θ to the bone edge will contribute a signal according to the trigonometric function $\arctan(\theta)$.

Gradient smoothing

The smoothed image I_{sC} is obtained by applying a Gaussian smoothing function G_{σ_s, σ_t} with standard deviations σ_s and σ_t to the gradient image I_{gC} :

$$I_{sC} = I_{gC} * G_{\sigma_s, \sigma_t}. \quad (11)$$

σ_t is the most important parameter of the entire algorithmic chain. It represents the assumption that local edges of an elongated bone do not vary significantly in the spatial direction parallel to its outer contour and that smoothing out edges parallel to this axis does not deteriorate the bone appearance much while at the same time suppressing any signal not originating from the target bone in the image. Setting $\sigma_t = 0$ mm would result in a bone image identical to the original image and thus in a void soft tissue image. Setting σ_t to a high value (e.g., 20 mm for human ribs) would result in a highly smoothed bone image with very low risk of including signals not originating from the target bone. On the other hand, such a parameter would not allow the bone model to reflect real variations in the signal intensity of the projected bone shadow along its contour well. These changes will stay in the soft tissue image. Visually, $\sigma_t = 5$ mm gives very accurate results; however, experiments have shown (see “Technical validation: the impact of bone suppression on lung nodule contrast” section) that also some edges belonging to lung tumors overlaid with a rib and oriented like its border may contribute to I_{sC} and thus get partially suppressed in the soft tissue image. Therefore, $\sigma_t = 20$ mm is preferred, despite the observation that the visual impression of the bone suppression quality is not optimal.

σ_s is set to 0 mm. Choosing a larger value would make the algorithm less vulnerable to segmentation errors. On the other hand, the bone model based on such a kernel in s -orientation will result in a blurred bone edge, thus leaving high frequency signals of the bone edge in the soft tissue image.

Reintegrate the gradient image

With the previous steps, the relevant information processing has been done already. I_{sC} represents the bone model. In the subsequent step, this image has to be transferred back into the original image space. The first step is to reintegrate intensity values from the partial derivatives coded in I_{sC} . The task is to compute

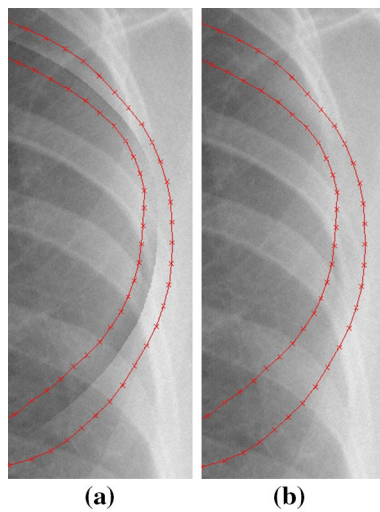


Fig. 8 The images illustrate the effect of the drift correction. In **a** no drift correction is applied, resulting in gray-value differences visible along the centerline of the fifth rib. **b** With drift correction, the bone is nicely suppressed. As a reference, the contour of the fifth rib is shown in red

$$I_{rc}(s, t) = \int_{s_0}^s I_{sc} I(i, t) di + I_{stc}(s_0, t). \quad (12)$$

The reintegration begins at the position s_0 , where the intensity is taken from the image I_{stc} . We use $s_0 = s_{\max}$ for this, thus starting at the outer margin and integrating inwards with decreasing s -values. So far, each line in the ST-image can be processed by (11) independently from the others. Processing a line is necessary only between $s_{\max} \geq s \geq c(t)$. At any position beyond the centerline, only *ghost images* can occur.

Drift correction

When it comes to retransformation of I_{rc} into the image space (see next subsection), method (12) may result in an artificial edge line along the centerline of the bone as visualized in Fig. 8. This is due to the fact that the transformation T_C has a singularity at the centerline. For a centerline position ($s = c(t_i), t_i$), we consider the local neighborhood ($s = c(t_i) + \Delta_s, t_i$) and may approximate ($s = c(t_i), t_i$) from both sides $\Delta_s < 0$ and $\Delta_s > 0$. As $c(t_i) < 0$ by definition, any $\Delta_s < 0$ means crossing the centerline. This we call approximation from the contralateral side. Any $\Delta_s > 0$ means not crossing the centerline, but staying ipsilateral. Therefore

$$\begin{aligned} \mathbf{p}_i &= \lim_{\Delta_s \rightarrow 0+} T_C \left(T_C^{-1}(s = c(t_i) + \Delta_s, t_i) \right) \\ &= (s = c(t_i), t_i), \Delta_s > 0 \\ \mathbf{p}_c &= \lim_{\Delta_s \rightarrow 0-} T_C \left(T_C^{-1}(s = c(t_i) + \Delta_s, t_i) \right) \\ &= (s = c(t_c), t_c), \Delta_s < 0 \end{aligned} \quad (13)$$

are different. The smoothing in (11) may result in $I_{rc}(\mathbf{p}_i) \neq I_{rc}(\mathbf{p}_c)$ which would not happen with $\sigma_s = \sigma_t = 0$. But with the necessary σ -setting, this results in the artificial edge line along the centerline of the bone (see Fig. 8).

The drift correction proposed here compensates for this effect by

$$I_{rc}^i(s, t) = I_{rc}(s, t) + \frac{I_{rc}(\mathbf{p}_c) - I_{rc}(\mathbf{p}_i)}{2} \times \left(1 - \frac{s - c(t)}{(s_{\max} - c(t))} \right)$$

and for I_{rc}^c respectively. This gives

$$\begin{aligned} I_{rc}^i(\mathbf{p}_i) &= I_{rc}(\mathbf{p}_i) + \frac{I_{rc}(\mathbf{p}_c) - I_{rc}(\mathbf{p}_i)}{2} \\ I_{rc}^c(\mathbf{p}_c) &= I_{rc}(\mathbf{p}_c) + \frac{I_{rc}(\mathbf{p}_i) - I_{rc}(\mathbf{p}_c)}{2}. \end{aligned}$$

$I_{rc}^l(\mathbf{p}_i) = I_{rc}^c(\mathbf{p}_c)$ is proven in the “Appendix.” The bone image in ST-space is therefore given by I_{rc} .

Transformation back into image space

The transformation of I_{rc} back into image space is performed in a straightforward manner by T_C^{-1} . But as I_{rc} may potentially have negative intensity values, which is physically implausible, these will be replaced by zero. The bone image I_{boneC} for the contour C is given by

$$I_{boneC}(x, y) = \max(I_{rc}(T_C(x, y)), 0). \quad (14)$$

Subsequent bone removals

The soft tissue image I_{softC} , where the bone C is suppressed, is given by

$$I_{softC}(x, y) = I(x, y) - I_{boneC}(x, y). \quad (15)$$

For a number of bone contours C_1, \dots, n , this operation is recursively applied by

$$\begin{aligned} I_{softC_0} &= I \\ I_{softC_i} &= I_{softC_{i-1}} - I_{boneC_i} \\ I_{soft} &= I_{softC_n}. \end{aligned} \quad (16)$$

The aggregated bone image is given by

$$I_{bone} = I - I_{soft} = \sum_{i=1}^n I_{boneC_i}. \quad (17)$$

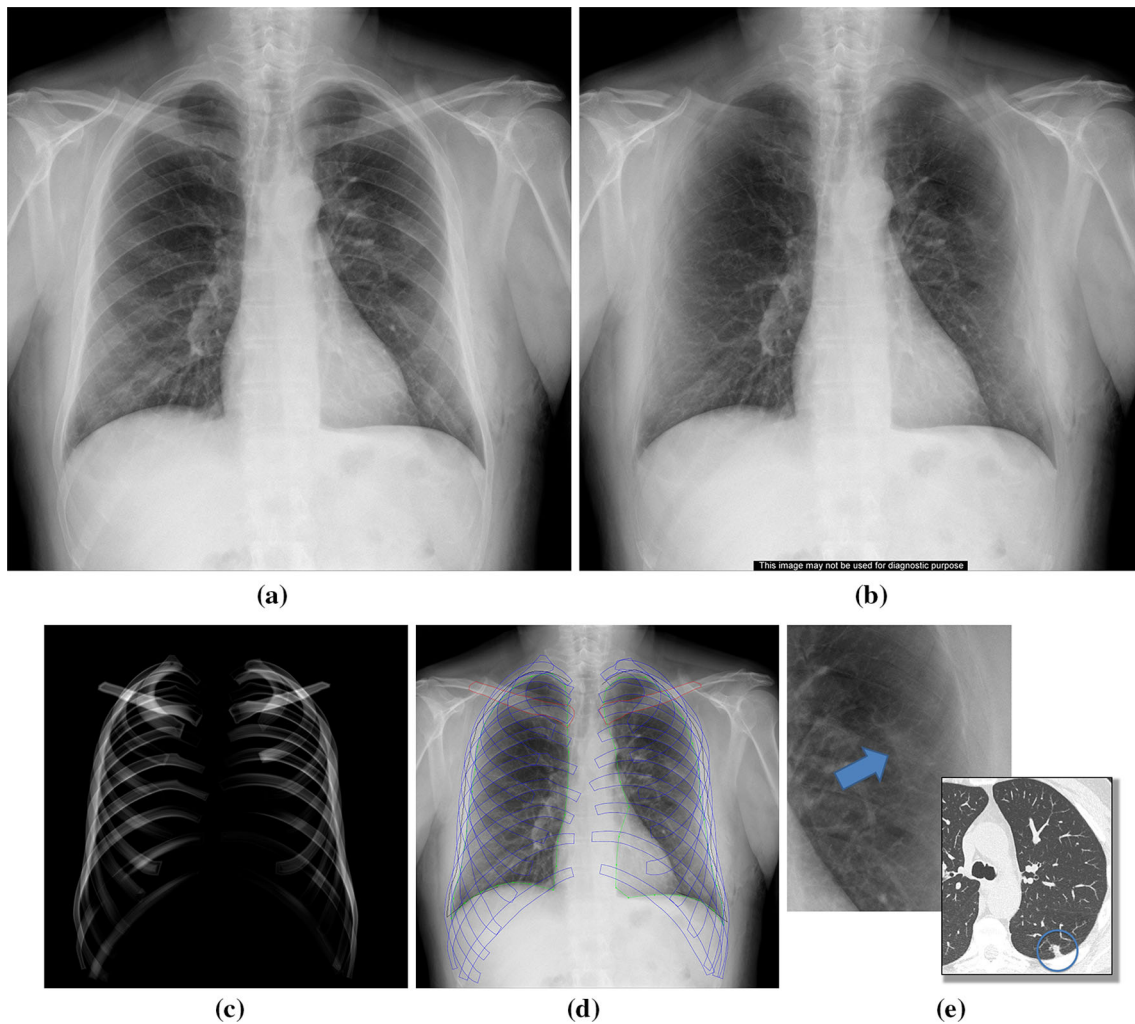


Fig. 9 A sample case with a lung nodule in the left lung field. Bone contours have been provided by manual delineation by one of the authors. Readers were more confident in detecting this nodule with bone sup-

pression than without. **a** Lung nodule case I . **b** Soft tissue image I_{soft} after processing. **c** Bone image I_{bone} . **d** All contours C_i used in bone suppression. **e** Nodule annotated in soft tissue image and in CT

Equation (17) holds only if the sequence of processing of the bones is kept. The order in $C_{1,\dots,n}$ does have an impact on I_{bone} and I_{soft} .

Example case

In Fig. 9, the complete I_{soft} and I_{bone} of a sample case are shown with $\sigma = 20$ mm. It is one of the positive cases used in the reader study with a lung nodule confirmed in CT. Readers were more confident in detecting a subtle nodule with bone suppression than without.

Technical validation: the impact of bone suppression on lung nodule contrast

In this section, an experiment is reported that was performed during the development and optimization of the bone sup-

pression algorithm. An additional clinical reader study is presented in the next section. In order to analyze the impact of our bone suppression method on the nodule contrast, we selected ten cases where a nodule of almost rib-sized diameter was located at the center of one rib. The nodules have been delineated in the original image by a contour C by use of the additional information from the soft image. In the following, the oriented contrast

$$c(\mathbf{p}) = \nabla I(\mathbf{p}) \mathbf{n}_C(\mathbf{p}) \quad (18)$$

is computed at the nodule contour.

$$c_{C,I} = \frac{1}{C_{\text{len}}} \int_{\mathbf{p} \in C} c(\mathbf{p}) d\mathbf{p} \quad (19)$$

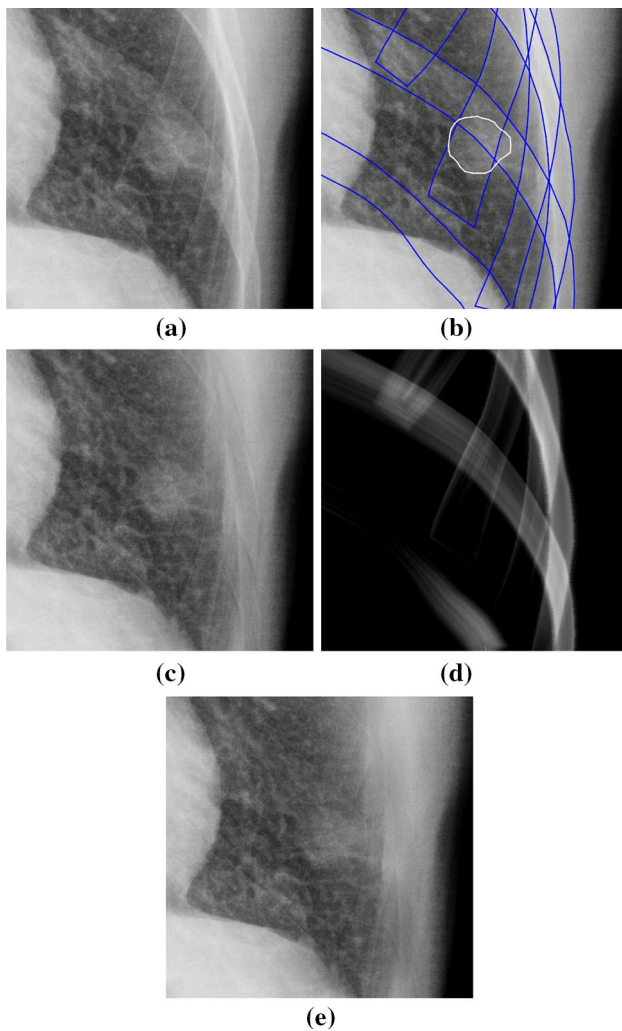


Fig. 10 A node with a contour congruent with a rib from case jpcln083 (a). Wherever the node contour (white) is close and almost parallel to a rib contour (blue in b), the task of separating a local edge in the original image I into a certain contribution from the node (I_{soft}) and another one from the bone (I_{bone}) is ill-posed. Using the preferred large kernel $\sigma_t = 20$ mm for bone suppression results in a visually appealing node impression in the soft image (c). The oriented contrast measured at the white contour hardly decreased between I and I_{soft} . Also the bone image (d) confirms this observation because there does not appear any signal originating from the node. In the rejected version with a smaller kernel $\sigma_t = 5$ mm, the contrast appears slightly reduced (e)

gives the average contrast for a nodule contour C . Note that negative and positive components may cancel out each other.

Nodule contrast needs to be preserved in order to sustain detectability. However, wherever a nodule edge is congruent with a bone edge, a distinction between the suppression of bone contrast and the suppression of nodule contrast is hardly possible. Figure 10 shows the contour of one of the selected nodules and how it is overlaid with the bone contours. Some parts of the nodule contour are congruent with a bone contour, others are not. At those locations being con-

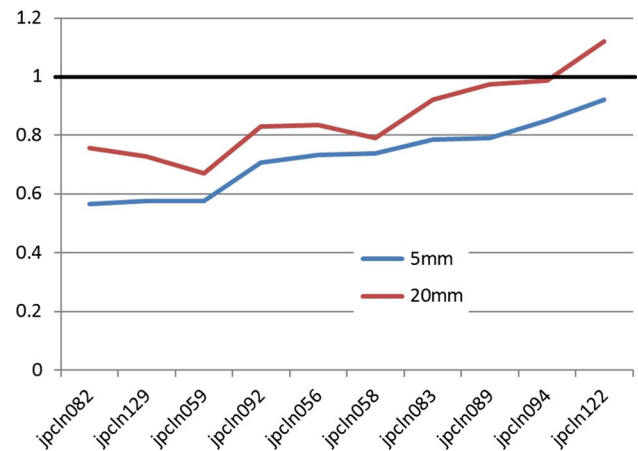


Fig. 11 Average node contrast c_C ratio (I_{soft}/I) for $\sigma_t = 5$ mm (blue) and $\sigma_t = 20$ mm (red) for all ten cases (sorted in ascending order by the $\sigma_t = 5$ mm-ratio). A value of 1 would mean no contrast change between I and I_{soft} . $\sigma_t = 20$ mm leads to higher values than $\sigma_t = 5$ mm does in all cases, which means a lower contrast loss by this kind of bone suppression. One case, jpcln122 actually has a contrast increased after bone suppression with $\sigma_t = 20$ mm

gruent, the nodule contrast decreased significantly after bone suppression. Initially, the images were processed with the parameter $\sigma_t = 5$ mm as this setting was assessed to provide the best visual bone suppression quality. The lower the value of σ_t gets, the higher gets the risk of also suppressing some nodule edges (see “Gradient smoothing” section). In Fig. 11, the ratio $\frac{c_{C, I_{\text{soft}}}}{c_{C, I}}$ is plotted for $\sigma_t = 5$ mm and for $\sigma_t = 20$ mm. The nodule contrast loss is clearly stronger when using $\sigma_t = 5$ mm, for $\sigma_t = 20$ mm it is close to zero.

From the results of this analysis, we may conclude that using a larger, more conservative kernel of $\sigma_t = 20$ mm to suppress bones preserves the nodule contrast much better than the kernel used before. For the reading study reported in the next section, this setting was used exclusively. A contrast loss of a nodule overlaid with a bone of 10 % has to be related to the contrast loss of the bone itself which is much stronger. Also, it should be considered that in this consideration a worst case scenario is examined that only concerns a subset of nodules. Those nodules whose outlines are not congruent with any rib contour are not reduced in contrast by the bone suppression algorithm.

Clinical validation

Ultimately, the benefit of bone suppression imaging for lung nodule detection should be demonstrated with a reader study comparing the performance of radiologists with and without additional soft images available. A study was performed at the radiology department of the Hospital Sant Pau in Barcelona, Spain. All procedures followed were in accor-

dance with the ethical standards of the responsible committee on human experimentation (institutional and national) and with the Helsinki Declaration of 1975, as revised in 2008. In order to better control the quality of segmentation of the thoracic bones, two different sessions with bone suppression have been performed. In one session, the soft image was based on contours of full ribs and clavicles segmented manually by the authors. Here, also the scapulae were included in case they were not properly located outside the lung field. In the other session, all contours were computed automatically with a method that will be published elsewhere. In general, the manual segmentations were more precise than the automatically determined contours.

Reading study design

The principal investigator selected the cases and established reference diagnostic labels for these Sant Pau cases by marking all lung nodules and confirm them in a chest CT image. He did not participate as reader. The two readers were experienced chest radiologist with more than 15 years of experience reading chest radiographs. They underwent a training session before with a limited number of cases not included in the study. For these cases, feedback was given on their detection performance. The study was held in four sessions in the order A, B, C, and D at different days, where the following readings were done:

- Two sessions with original image only, 1 month apart (A, C)
- Original image plus semi-automatic bone suppressed image (contours segmented manually) side by side (B)
- Original image plus automatic bone suppressed image (contours segmented automatically) side by side (D)

The order of images was randomized again for each session. Images were read under typical conditions in the reading room, and readers used a side-by-side presentation of both images on different monitors in session B and session D. The readers were asked to report their findings on prepared sheets. Nodule locations were indicated by an enclosing circle on a printout of the original X-ray, and the confidence levels regarding the presence or absence of a lung nodule were rated at six defined levels: 0 (definitely no nodule), 1, 2 (probably no nodule), 3, 4 (probably nodule), 5, 6 (definitely nodule). No feedback was provided to the readers. The set of 146 cases originated from the Hospital Sant Pau (68 cases), the Japanese public database JSRT [20]¹ (63 cases), and the US public database LIDC [2]² (15 cases). Fifty-eight of those

were healthy control subjects, and 88 were subjects with one or more pulmonary nodules. A selection of cases was made to include nodules of a particular level of subtlety. For the JSRT cases, this was subtlety levels 3 and 4. For the other cases, no explicit subtlety rating was available. Nodules were restricted to be located in the lung fields excluding the retrocardial area, the area below the diaphragm, and the mediastinum. There was a total of 123 nodules in the data set, and 25 % of the cases showed foreign bodies such as electrodes, tubes, or even one pacemaker that potentially could complicate the automatic image processing.

Results

Reading the additional soft image in sessions B and D took about 25 % more reading time when compared to the initial image alone in sessions A and C. Since the task stated to the readers was to detect all visible nodules, the method applied to calculate false nodule detection rates and specificity values should be clearly defined. In the following, the analysis is separated into a first part documenting detection rates and a second part on ROC analysis. Here, false positive rates are given by dividing the number of false detected nodules by the total number of images, which appears intuitive. In addition, a complete ROC analysis is presented where all six confidence thresholds are included. Here, in order to stay within the ROC paradigm, false positive rates (named “1-specificity” in this context) are calculated by dividing the number of false detected nodules by the negative nodule sample size. This is detailed below.

Detection rates

Based on the findings, detection rates and false positive rates could be determined considering all confidence ratings unequal 0 (definitively no nodule) as a detection. Detection rate was given by the number of localized true positive nodules divided by the number of nodules (123), while the false positive rate was the total number of any false detected nodule divided by the number of images (146) here. False nodules were counted in images without nodules, as well as in images containing nodules but which were marked at different locations. Baseline rates (no bone suppression) were averaged over session A and session C here. For reader I, the results were as follows

- The nodule detection rate increased from 46.7 to 52.0 % with semi-automatic bone suppression.
- The nodule detection rate increased from 46.7 to 51.2 % with automatic bone suppression.
- The false positive rate decreased from 0.23 to 0.21 per image with semi-automatic bone suppression.

¹ Images publicly available from <http://www.jsrt.or.jp/jsrt-db/eng.php>.

² Images publicly available from <http://cancerimagingarchive.net>.

- The false positive rate was stable at 0.23 with automatic bone suppression.

For reader II, the results were as follows

- The nodule detection rate increased from 48.0 to 48.8 % with semi-automatic bone suppression.
- The nodule detection rate stayed constant at 48.0 % with automatic bone suppression.
- The false positive rate decreased from 0.25 to 0.12 per image with semi-automatic bone suppression (50 % reduction).
- The false positive rate decreased from 0.25 to 0.16 per image with automatic bone suppression (40 % reduction).

Given these numbers, both readers could benefit from the bone suppression technique: reader I more with respect to detection rate and reader II more with respect to false positive rate. Still, every comparison itself shows a positive stable trend and thus demonstrates an advantage of the bone suppression method. A really encouraging factor is that the false positive rate did not increase. This is in contrast to all other studies in the literature, where despite an overall gain in the area under the ROC curve the specificity decreased.

ROC curves

In order to generate a receiver operating characteristic (ROC) curve on nodule detection and localization for a reader on a nodule basis, the number of negative nodule samples (i.e., the denominator in the specificity calculation) was set to contain every false location (be it in a positive or in a negative image) that has been marked by the reader in at least one of the four sessions. For this purpose, when two marks on separate sheets were recorded, a decision was made after visual assessment whether or not these marks referred to the same image location. In addition, every negative image that has never been marked by the reader counted as negative nodule sample, too. This amounts to 62 occasionally marked positions plus 42 images that were never marked for reader I and 65 occasionally marked positions plus 37 images that were never marked for reader II. In the ROC curves, 1-specificity is therefore given by the number of false detected nodules divided by the negative sample size of 104 (62 + 42 for reader I) and 102 (65 + 37 for reader II) instead of the number of cases (146) that was used in the previous section about rates. The positive sample size determining sensitivity is given again by the number of true nodules (123) equally for both readers.

Figure 12 shows the ROC curves for both readers. For reader I, the area under the ROC curve (AUC) increased from 0.596 to 0.642 from session A to session B and from 0.609 to 0.622 from session C to session D. For reader II, AUC increased from 0.593 to 0.667 from session A to ses-

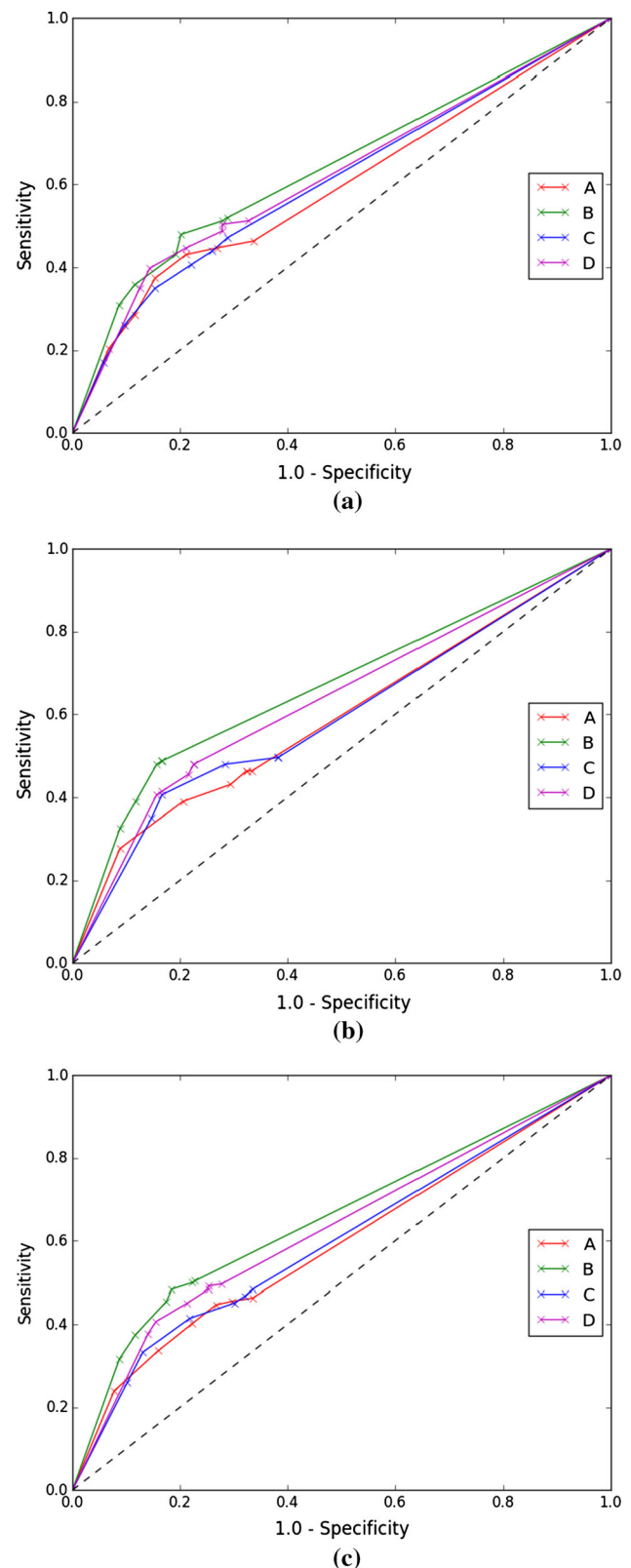


Fig. 12 ROC curves of the lung nodule detection and localization study. Sessions: A no bone suppression, B bone suppression based on manually segmented contours, C no bone suppression again, D bone suppression based on automatically segmented contours. **a** Reader I. **b** Reader II. **c** Pooled data

Table 1 Pairwise comparison of session results for pooled readers: difference in AUC and its *P* value

Session	A	B	C	D
A	–			
B	0.062 (1.95 %)	–		
C	0.007 (73 %)	0.055 (0.77 %)	–	
D	0.036 (9.16 %)	0.026 (15.76 %)	0.029 (18.51 %)	–

Significantly different session pairs ($P < 5\%$) have bold entries

sion B and from 0.595 to 0.635 from session C to session D. In the pooled data of both readers, AUC increased from 0.593 to 0.655 from session A to session B and from 0.600 to 0.628 from session C to session D. The pairwise comparisons on all sessions are shown in Table 1. Significant differences between sessions can be observed following [3] between A and B and between B and C. This means there is a significant improvement in nodule detection when using our bone suppression method based on the semi-automatically segmented bones, and a less pronounced one based on the automatically segmented bones. The repetition of session A conditions in session C resulted in a very similar response of the readers.

Case selection

Designed as an initial study, the subtlety range of the data set was not very narrow. A significant portion of nodules (37 %) were consistently not detected by any reader in any session. Others (7 %) have been rated to be definitely a nodule by both readers in all four sessions (with and without bone suppression). As there was no subtlety rating available for all cases for a prospective analysis of subtlety subgroups, we excluded these two groups of nodules in a retrospective analysis. Once all these nodules being either too obvious or too subtle both by means of bone suppression or without are excluded, AUC increases from 0.629 to 0.749 between session A and session B and from 0.645 to 0.704 between session C and session D. The difference between bone suppression and not bone suppression becomes more expressed based on the reduced data set. However, with this retrospective operation, the significance levels do not change with respect to the full data set. Figure 13 shows the same ROC curves as Fig. 12 does, but for the reduced interesting data set only. Comparing session A with B and session C with D in the ROCs confirms the observation of a clear benefit of our bone suppression, both in the automatically and in the semi-automatically processed images.

Discussion

A novel method was introduced to suppress bone shadows in radiographs from given contours of the ribs. Its parameters were optimized to increase the visibility of subtle lung

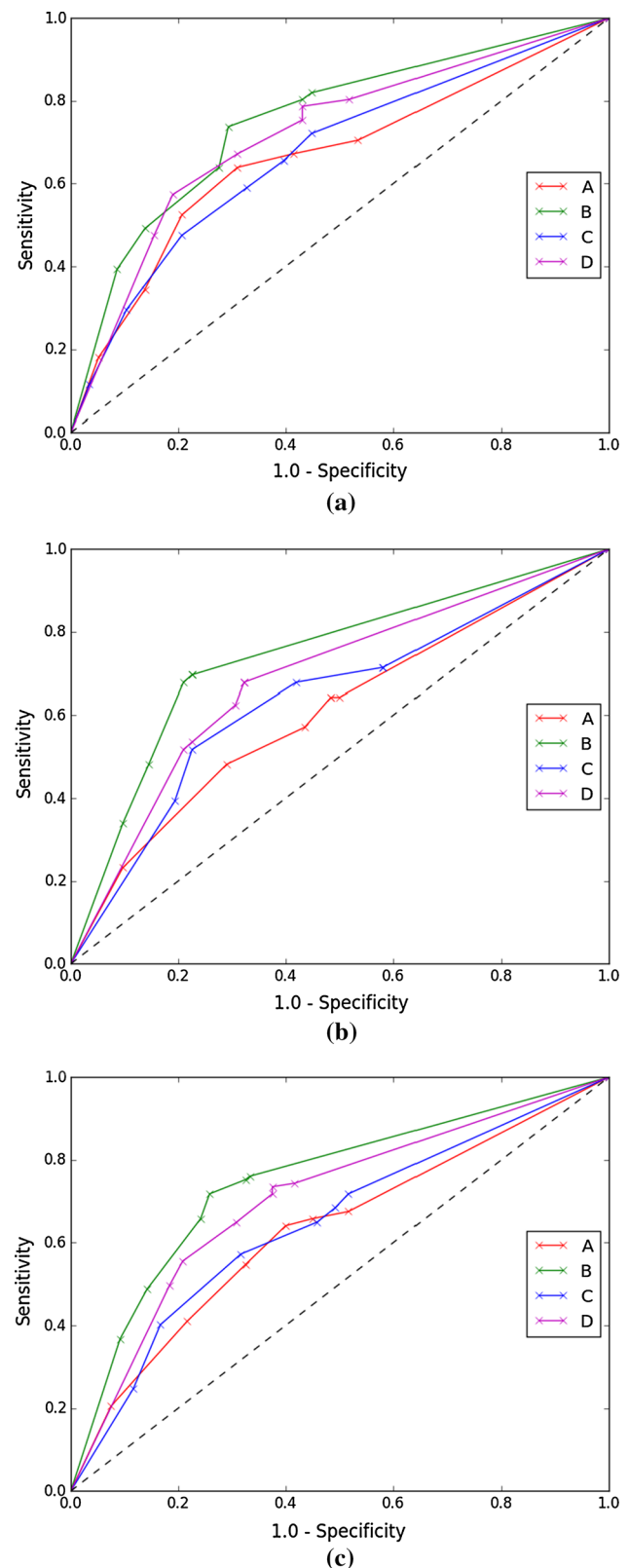


Fig. 13 ROC curves after case selection. Sessions: A no bone suppression, B bone suppression based on manually segmented contours, C no bone suppression again, D bone suppression based on automatically segmented contours. **a** Reader I. **b** Reader II. **c** Pooled data

nodules and to leave the image unaffected apart from the suppression of bone contrast.

Suppression accuracy

While analyzing the influence of the most important parameter, a tradeoff was encountered between nodule visibility and bone suppression accuracy if both overlap and have congruent edges. A conservative parameter value was chosen for the study that optimizes nodule visibility. Alternative parameter settings to the one used here may yield a more visually appealing suppression of the bone signal, but with a potential impact upon the visibility of some nodules, as discussed above in “Technical validation: the impact of bone suppression on lung nodule contrast” section.

Study design

A significant benefit of bone suppression could be shown by a reader study on lung nodule detection and localization as reported earlier in this text. With two experienced readers who benefitted from the method but also responded differently compared to each other, it is hard to draw conclusions on different reader types. The number of cases, however, may be considered sufficient and resulted in statistically significant results at least for the manually delineated bones in session B. The study setup was different to other referenced publications as every nodule had to be identified by the reader. Other studies typically included a single nodule only per case, or they let the reader rate the most obvious nodule only. In the study reported here, localization of nodules in the image was necessarily required. A mark in a case containing a true nodule at a distant location was counted as false positive. This design decision was taken in order to assess nodule visibility directly rather than reflecting clinical decision taking on a case basis. Consequently, both detection rates and sensitivity were related to the number of nodules (123), while false positive rates were related to the number of images (146). In order to get a valid description of the ROCs, specificity was related to the number of negative nodule cases (104 and 102 for the two readers). Of course, method and parameters were equally applied to all four sessions making them comparable.

Case selection

This study is the first one to use this novel bone suppression technique. For this purpose, the selection criterion on nodule subtlety was broadly defined in order to avoid an excessively exclusive nodule type selection. *Soft images* were not used for case selection. Consequently, nodules which were hardly visible, or even not visible in the original radiograph (but detected in CT), have been included in the study, because they may be visible in the *soft images*. This, how-

ever, also caused a high number of nodules (37 %) that have not been detected by any of the two readers in any of the four sessions each. Unfortunately, a consistent baseline subtlety rating was not available that would have allowed for a separate analysis of different subtlety classes. As a substitute for this, the retrospective case selection was performed in addition to the general analysis. Here, these invisible nodules, but also those being consistently considered definitively a nodule were retrospectively excluded from analysis. This was done in order to demonstrate that case selection can have a significant impact on the study result. Importantly, the significance values reported in our results relate to the analysis of the full data set (and in any case, the retrospective case selection described above does not impact the significance calculation).

Apart from the study results, some additional qualitative observations on the performance of bone suppression are demonstrated and discussed below. A focus is set to particular challenging anatomical regions and extraordinary imaging conditions. All presented soft image examples are based on manually segmented bone contours that have been used in session B of the study.

Overlapping anatomical contours

Our bone suppression method integrates specifically oriented image gradients along the bone contour with a wide kernel of several centimeters. Therefore, strongly contrasted edges crossing the bone may potentially cause image artefacts. Such edges typically originate from the diaphragm, the cardiac border, other bones, the female breast, to name the most important ones. These edges might be integrated into the *bone image* of a given bone and thus suppress these respective structures in the *soft image* in addition to the target bone. Figure 14 shows a region of interest around a lung nodule in the right lung base. The ribs in this region partly cross the diaphragm, the lateral lung border, and the lower lateral border of the female breast. Still, none of these edges appear visible in the *bone image*. Therefore, these edges do not appear artificially suppressed in the *soft image* after subtraction.

Foreign bodies

Foreign bodies may also result in strongly contrasted edges overlaid with the lung field of a chest radiograph. Similar to the contours caused by normal anatomy, but with even higher contrast, they are a potential source of artefacts for bone suppression. Foreign body images were not generally excluded from the study. Figure 15 shows the most severe foreign body in the study, a pacemaker in the upper left lateral lung field with a cable crossing the left lung and the clavicle and ribs located there. Even these strongly contrasted edges caused

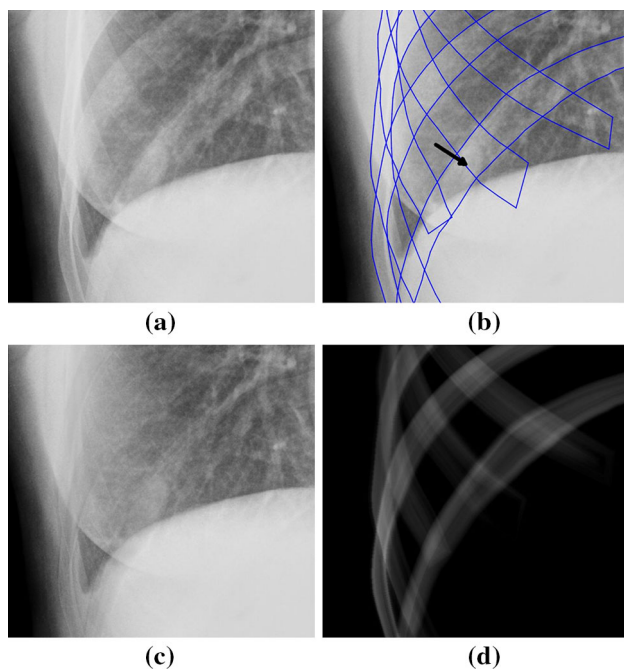


Fig. 14 Detailed view onto a lung nodule case (a). The nodule is covered by a rib and located close to other highly contrasted contours such as the diaphragm and the female breast that overlap with the bones. Rib segmentations are shown in b, and the nodule center is also marked there for the reader's convenience. The overlaid contours do not appear to have a negative impact on the separation of the image I into its two components I_{soft} (c) and I_{bone} (d)

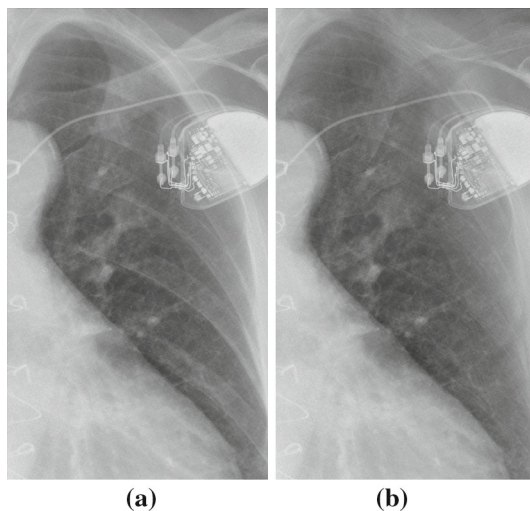


Fig. 15 A detail from one of the foreign body cases: a pacemaker appears overlaid with some ribs. It does not appear affected by the bone suppression, while the overlaid ribs are significantly decreased in contrast. Also the cable overlaid with a clavicle and some ribs remain well contrasted. a Original case (detail) with pacemaker. b Soft tissue image after processing

by metal parts do not interfere significantly with the suppression of the overlaid bones and thus do not cause remarkable artefacts visible in the *soft image*.

Abnormal thoracic anatomy

It is interesting to observe how bone suppression processes cases with some abnormal skeletal signs such as rib fractures or calcifications. Unlike dual-energy subtraction, our bone suppression method does not separate the signal by the physical properties of different tissue types. It models absorption properties of a typical bone smoothly along its contour. Deviations from that like fractures or cysts are not integrated into the bone model and thus show up in the *soft image* instead of the *bone image*, which makes this term a little bit imprecise. Some readers confronted with this fact were initially confused, especially those with previous experience with dual-energy subtraction imaging. However, to the majority of radiologists it appeared beneficial for the diagnosis that abnormal signs remain in the *soft image*, while all normal thoracic bones tend to diminish. We did not encounter obvious fractures in the data set of our study, but an abnormal sign that can be frequently observed is calcified cartilage. In Fig. 16, it is demonstrated how such an abnormal skeletal sign is processed. The calcification of a costochondral joint is not modeled as bone and thus remains in the *soft image*. The readers of our study have been exposed to this effect in the training session, so they were prepared for it in the study. The remaining calcification of the first rib joint may

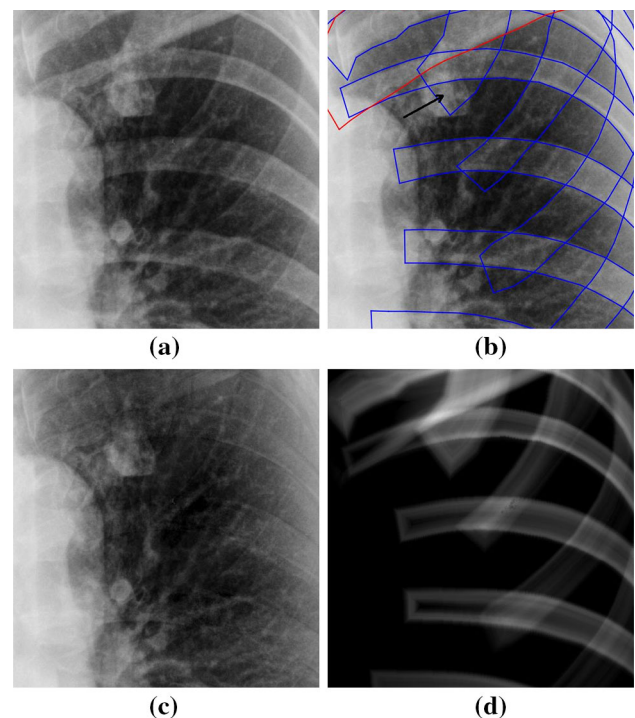


Fig. 16 Detailed view onto a normal case (a). The cartilage of the costochondral joint of the first left rib appears calcified (see arrow). As bone suppression works on the normal rib contour, b the calcification outside the rib substantially remains in the *soft image* (c) and not in the *bone image* (d)

appear very similar to a lung nodule. This effect accounted for a number of false positive findings in the study. For the specific case shown in Fig. 16, false detection incidence did not increase when using additional bone suppression in the study.

Conclusion

A novel method is presented that allows the automatic suppression of single bones in radiographs based on their contours. Applied to all ribs and clavicles in a chest posterior–anterior radiograph, this method provides a soft image where important soft tissue-related findings may no longer be obscured by bone shadows. In an observer study with two experienced radiologists, such an additional soft image increased the area under the ROC curve for a solid lung nodule detection and localization task significantly from 0.637 (average of the two identical baseline sessions A and C without bone suppression) to 0.749 (session B with bone suppression). For this evaluation, all obvious and all invisible nodules have been removed from the analysis. This means both readers concurred with each other in their confidence in all four sessions to be either always definitively no nodule (0) or definitively a nodule (6). Without this restriction, the increase in the AUC on the total of 146 cases from 0.596 to 0.655 is still significant. Not only the detection rate (sensitivity) increased for both readers, but also the false positive rate decreased (specificity increased) for both readers. One reader benefited more with respect to its sensitivity, while the other benefited more with respect to its specificity. In contrast to that, all previously published reader studies on bone suppression for lung nodule detection agreed in a reduction of their readers' specificity, while the sensitivity increased with their bone suppression. Even though the number of readers in our study may not be sufficiently high to draw final conclusions, we contribute this fact to the specific way our bone suppression methods process the images. It is designed to do as little modification to the image as necessary to suppress bone shadows. Being an explicit method representing each bone, every pixel outside the range of any bone contour is unaffected, such that the intercostal space is not processed at all.

The novel bone suppression method proposed in this paper showed a significant improvement in a lung nodule detection and localization task with over one hundred cases and two experienced readers. Generally, both the sensitivity and the specificity of the readers benefitted from it. Using bone suppression in chest radiography reading may thus help detecting a significant rate of lung cancer cases earlier without a burden of more false positive findings. The method has a specific benefit regarding the detection of subtle lung nodules that become visible once the overlaid bones are suppressed.

Acknowledgments We would like to thank Martin Haker and Moritz Schaar, both former employees of Philips Research Hamburg, for their algorithmic contribution. We also would like to thank Raoul Florent and Claire Levrier, Philips Medisys, Paris and Harald Heese, Philips Research Hamburg, for some valuable suggestions. We are grateful to Cornelia Schaefer-Prokop, Meander Medical Center Amersfoort, the Netherlands, and Martin Uffmann, Landesklinikum Neunkirchen, Austria, for their assessments in the early phases of the project. We would like to thank C. A. Nuñez at Hospital Sant Pau, Barcelona, for her support in preparing the reader study.

Compliance with ethical standards

Conflict of interest J. von Berg, S. Young, H. Carolus, A. Saalbach, and R. Wolz are employees of Philips. A. Hidalgo, A. Giménez, and T. Franquet do not have a conflict of interest.

Appendix

In order to prove that

$$I_{rc}^l(\mathbf{p}_i) \stackrel{?}{=} I_{rc}^c(\mathbf{p}_c)$$

we set

$$\begin{aligned} I_{rc}(\mathbf{p}_i) + \frac{I_{rc}(\mathbf{p}_c) - I_{rc}(\mathbf{p}_i)}{2} \\ \stackrel{?}{=} I_{rc}(\mathbf{p}_c) + \frac{I_{rc}(\mathbf{p}_i) - I_{rc}(\mathbf{p}_c)}{2} \\ I_{rc}(\mathbf{p}_i) - I_{rc}(\mathbf{p}_c) \\ \stackrel{?}{=} \frac{I_{rc}(\mathbf{p}_i) - I_{rc}(\mathbf{p}_c) - (I_{rc}(\mathbf{p}_c) - I_{rc}(\mathbf{p}_i))}{2} \\ I_{rc}(\mathbf{p}_i) - I_{rc}(\mathbf{p}_c) = I_{rc}(\mathbf{p}_i) - I_{rc}(\mathbf{p}_c) \end{aligned}$$

which proves the convergence of I_{rc}^i and I_{rc}^c at the centerline.

Informed consent was obtained from all patients for being included in the study.

References

- Ahmed B, Rasheed T, Khan MA, Cho SJ, Lee S, Kim TS (2007) Rib suppression for enhancing frontal chest radiographs using independent component analysis. In: Beliczynski B, Dzielski A, Iwanowski M, Ribeiro B (eds) Adaptive and natural computing algorithms. Springer, Berlin, pp 300–308
- Armato SG III, McLennan G, Bidaut L, McNitt-Gray MF, Meyer CR, Reeves AP, Zhao B, Aberle DR, Henschke CI, Hoffman EA, Kazerooni EA, MacMahon H, van Beek EJR, Yankelevitz D, Biancardi AM, Bland PH, Brown MS, Engelmann RM, Laderach GE, Max D, Pais RC, Qing DPY, Roberts RY, Smith AR, Starkey A, Batra P, Caligiuri P, Farooqi A, Gladish GW, Jude CM, Munden RF, Petkovska I, Quint LE, Schwartz LH, Sundaram B, Dodd LE, Fenimore C, Gur D, Petrick N, Freymann J, Kirby J, Hughes B, Castele AV, Gupte S, Sallam M, Heath MD, Kuhn MH, Dharaiya E, Burns R, Fryd DS, Salganicoff M, Anand V, Shreter U, Vastagh S, Croft BY, Clarke LP (2011) The lung image database consortium (LIDC) and image database resource initiative (IDRI): a completed reference database of lung nodules on ct scans. *Med Phys* 38(2):915–931

3. DeLong ER, DeLong DM, Clarke-Pearson DL (1988) Comparing the areas under two or more correlated receiver operating characteristic curves: a nonparametric approach. *Biometrics* 44:837–845
4. Freedman MT, Lo SCB, Seibel JC, Bromley CM (2011) Lung nodules: improved detection with software that suppresses the rib and clavicle on chest radiographs. *Radiology* 260(1):265–273
5. Hogeweg L, Sanchez C, van Ginneken B (2013) Suppression of translucent elongated structures: applications in chest radiography. *IEEE Trans Med Imaging* 32(11):2099–2113
6. Hogeweg LE, Mol C, de Jong PA, van Ginneken B (2010) Rib suppression in chest radiographs to improve classification of textural abnormalities. In: *Proceedings of the SPIE medical imaging*, vol 7624
7. Horváth Á, Orbán GG, Horváth Á, Horváth G (2013) An X-ray CAD system with ribcage suppression for improved detection of lung lesions. *Electr Eng Comput Sci* 57(1):19–33
8. Horváth G, Orbán G, Horváth Á, Simkó G, Pataki B, Máday P, Juhász S (2009) A CAD system for screening X-ray chest radiography. In: *World congress on medical physics and biomedical engineering*, September 7–12, 2009, Springer, Munich, Germany, pp 210–213
9. Kim S, Pyo HB, Lee SK, Lee S, Park SH (2000) Digital image subtraction of temporally sequential chest images by rib image elimination. In: *Proceedings of the 22nd annual international conference of the IEEE engineering in medicine and biology society*, vol 3. IEEE, pp 1752–1755
10. Lee JS, Wang JW, Wu HH, Yuan MZ (2012) A nonparametric-based rib suppression method for chest radiographs. *Comput Math Appl* 64(5):1390–1399
11. Li F, Engelmann R, Pesce L, Armato SG III, MacMahon H (2012) Improved detection of focal pneumonia by chest radiography with bone suppression imaging. *Eur Radiol* 22(12):2729–2735
12. Li F, Engelmann R, Pesce LL, Doi K, Metz CE, MacMahon H (2011) Small lung cancers: improved detection by use of bone suppression imaging—comparison with dual-energy subtraction chest radiography. *Radiology* 261(3):937–949
13. Lo SCB, Freedman MT (2012) Changes of nodule detection after radiologists read bone opacity suppressed chest radiography. In: *SPIE medical imaging. International Society for Optics and Photonics*, pp 83152S–83152S
14. Loog M, van Ginneken B, Schilham AM (2006) Filter learning: application to suppression of bony structures from chest radiographs. *Med Image Anal* 10(6):826–840
15. Novak RD, Novak NJ, Gilkeson R, Mansoori B, Aandal GE (2013) A comparison of computer-aided detection (CAD) effectiveness in pulmonary nodule identification using different methods of bone suppression in chest radiographs. *J Digit Imaging* 26(4):651–656
16. Orbán G, Horváth Á, Horváth G (2010) Lung nodule detection on rib eliminated radiographs. In: *XII mediterranean conference on medical and biological engineering and computing 2010*. Springer, pp 363–366
17. Schalekamp S, van Ginneken B, van den Berk IAH, Hartmann IJC, Snoeren MM, Odink AE, van Lankeren W, Pegge SAH, Schijf LJ, Karssemeijer N, Schaefer-Prokop CM (2014) Bone suppression increases the visibility of invasive pulmonary aspergillosis in chest radiographs. *PLoS One* 9(10):e108551
18. Schalekamp S, van Ginneken B, Meiss L, Peters-Bax L, Quekel LG, Snoeren MM, Tiehuis AM, Wittenberg R, Karssemeijer N, Schaefer-Prokop CM (2013) Bone suppressed images improve radiologists detection performance for pulmonary nodules in chest radiographs. *Eur J Radiol* 82(12):2399–2405
19. Shah PK, Austin JH, White CS, Patel P, Haramati LB, Pearson GD, Shiau MC, Berkmen YM (2003) Missed non-small cell lung cancer: radiographic findings of potentially resectable lesions evident only in retrospect 1. *Radiology* 226(1):235–241
20. Shiraishi J, Katsuragawa S, Ikezoe J, Matsumoto T, Kobayashi T, Komatsu K, Matsui M, Fujita H, Kodera Y, Doi K (2000) Development of a digital image database for chest radiographs with and without a lung nodule: receiver operating characteristic analysis of radiologists' detection of pulmonary nodules. *Am J Roentgenol* 174(1):71–74
21. Simkó G, Orbán G, Máday P, Horváth G (2009) Elimination of clavicle shadows to help automatic lung nodule detection on chest radiographs. In: *4th European conference of the international federation for medical and biological engineering*. Springer, pp 488–491
22. Suzuki K, Abe H, MacMahon H, Doi K (2006) Image-processing technique for suppressing ribs in chest radiographs by means of massive training artificial neural network (MTANN). *IEEE Trans Med Imaging* 25(4):406–416
23. Szucs-Farkas Z, Schick A, Cullmann JL, Ebner L, Megyeri B, Vock P, Christe A (2013) Comparison of dual-energy subtraction and electronic bone suppression combined with computer-aided detection on chest radiographs: effect on human observers' performance in nodule detection. *Am J Roentgenol* 200(5):1006–1013
24. Tanaka R, Sanade M, Oda M, Suzuki M, Sakuta H, Kawashima H, Iida H (2013) Improved accuracy of IGRT with bone suppression image-processing. *Int J CARS* 8(suppl 1):41
25. Vogelsang F, Weiler F, Dahmen J, Kilbinger M, Wein B, Günther R (1998) Detection and compensation of rib structures in chest radiographs for diagnose assistance. In: *Proceedings of the international symposium on medical imaging*, vol 3338, p 1